

# Occurrence Characteristics of Water in Nano-Slit Pores under Different Solution Conditions: A Case Study on Kaolinite

Zhiyan Zhou, Junqian Li,\* Zhaojing Song, and Rixin Zhao


Cite This: *ACS Omega* 2023, 8, 18990–19001

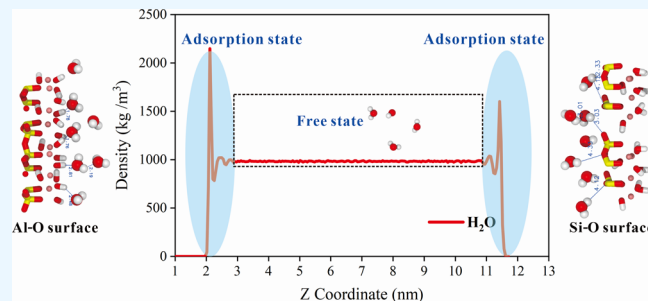

Read Online

ACCESS |

Metrics &amp; More

Article Recommendations

**ABSTRACT:** The presence of water in narrow pore spaces affects the occurrence and flow of methane, which in turn affects shale gas production. Therefore, studying the occurrence and distribution characteristics of water is of great significance to predict gas production. Based on molecular dynamics simulations, this study investigated the occurrence characteristics and influencing variables of liquid water in kaolinite nanopores *in situ*. Owing to its widespread distribution, kaolinite is the most prevalent clay mineral with two surfaces with different characteristics. Three systems of pure water, a  $\text{CaCl}_2$  solution, and a  $\text{H}_2\text{O}/\text{CH}_4$  mixed phase were created at varied temperatures ( $80\text{--}120^\circ\text{C}$ ) and pressures ( $70\text{--}120\text{ MPa}$ ). The presence of gas and water in the nanopores was investigated thoroughly. The results showed that the adsorption of water on the Al–O octahedral surface of kaolinite was not affected by external conditions under *in situ* conditions, whereas the adsorption of water on the Si–O tetrahedral surface decreased with increasing temperature, but the change was small. When ions were present in the system, the water capacity decreased. Based on the aforementioned results, external conditions, such as temperature and pressure do not affect the basic state of water. However, if there are more than two fluid types in the system, the adsorption of water on the mineral surface is reduced owing to competitive adsorption. In addition, a  $\text{CH}_4\text{--H}_2\text{O}$  mixed system was simulated, in which methane molecules were distributed in clusters. There are two types of adsorptions in pores: gas–solid interactions and solid–liquid–gas interactions.  $\text{CH}_4$  molecules are thought to be clustered in water molecules because of the strong hydrogen bonding interactions among the water.



## 1. INTRODUCTION

With progress in exploration technology and the gradual breakthrough of targeted theories, the exploration and development of unconventional oil and gas in China have made significant progress.<sup>1–4</sup> Shale gas is one of the hot spots at the forefront of oil and gas research and exploration, and the related study is mainly focused on the marine shale of the Lower Silurian Longmaxi Formation in the Sichuan Basin, China.<sup>5–9</sup> However, marine shale in southern China has a complex water-bearing condition, which results in two main aspects of reservoir water: (1) *in situ*, there is widespread water in shale reservoirs,<sup>10–12</sup> and (2) hydraulic fracturing technology has become an indispensable tool in shale gas development. Fracturing fluid retention also results in shale gas reservoirs containing a certain amount of water.<sup>13–16</sup> According to previous studies, the water saturation of the marine shale in southern China ranges from 30 to 95%.<sup>17</sup> Combined with the production data, it was found that there was a negative correlation between the water content and gas content.<sup>17,18</sup> The presence of water in a formation is an important factor affecting the production of shale gas.

How does formation water affect shale gas exploitation? Several experimental studies have been conducted on this

topic. Gasparik et al.<sup>19,20</sup> found that the methane adsorption capacity of wet shale was approximately 40–90% lower than that of dry shale. Han et al.<sup>21</sup> experimentally found that the higher the water content of shale, the lower its methane adsorption capacity. Some scholars studied the water vapor adsorption law by water vapor adsorption experiments under different temperature and pressure conditions, and established adsorption models.<sup>22–25</sup> Previous experiments on water vapor adsorption have emphasized the influence of water vapor on shale gas adsorption and fluid flow capacity.<sup>22–28</sup> However, it is controversial whether water is gaseous under formation conditions, and some studies have shown that the water phase is liquid under high-temperature and high-pressure conditions at certain burial depths.<sup>29</sup> In the liquid state, intermolecular forces exist between the water molecules,

Received: March 10, 2023

Accepted: May 4, 2023

Published: May 16, 2023



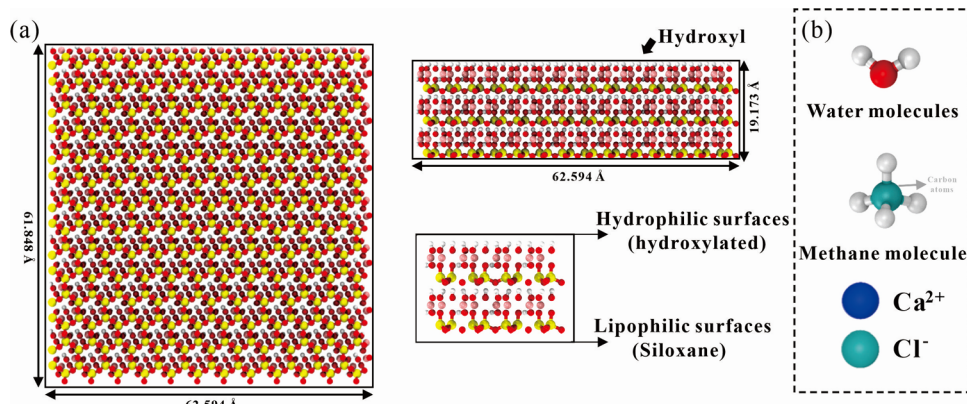


**Figure 1.** Initial conformation diagram of (a) kaolinite supercell structure, (b) water molecules, methane molecules,  $\text{Ca}^{2+}$ , and  $\text{Cl}^-$ .

including van der Waals forces and hydrogen bonding. Owing to hydrogen bonding, water molecules may link to form molecular associations, whereas gaseous water molecules do not exist.<sup>30</sup> Therefore, the distribution characteristics of water obtained from the water vapor adsorption experiments are quite different from those of liquid water. It is important to study the occurrence and distribution characteristics of liquid water, which are of great significance for predicting reservoir capacity and gas production.

In addition, some scholars have studied the occurrence of methane and water in pores. In shale reservoirs, water is primarily stored in clay minerals rather than organic minerals.<sup>31–34</sup> Moreover, clay minerals play an important role in  $\text{CH}_4$  adsorption.<sup>35–37</sup> Therefore, studying the interactions between clay minerals and water is crucial. Zolfaghari et al.<sup>38</sup> suggested that the composition of clay minerals in shale directly determines the strength of the water adsorption capacity. Wang et al.<sup>39</sup> found that the clay mineral content of clay-rich shale has an important influence on  $\text{CH}_4$  adsorption. Some scholars have concluded that the adsorption of  $\text{CH}_4$  by clay minerals in shale cannot be neglected, and the adsorption ratio can be as high as 44.12%, especially in shales with low organic content, where the adsorption of clay minerals plays a cardinal role. Under experimental conditions, the influence of the clay mineral type on the  $\text{CH}_4$  adsorption capacity was in the following order: montmorillonite > kaolinite > illite.<sup>27,35,40</sup> Kaolinite is one of the most common components of clay minerals and has an octahedral structure with 1:1 structural unit layers.<sup>41,42</sup> The Si–O tetrahedral and Al–O octahedral surfaces of the kaolinite layers have different hydrophilicity and hydrophobicity. Therefore, it is important to understand the behavior of water in kaolinite pores to study clay mineral–water interaction systems.<sup>43</sup>

However, it is difficult to understand the microscopic interaction characteristics of water in clay minerals through experimental studies of the distribution characteristics of water in clay minerals and the competitive adsorption of gaseous water. Recently, molecular dynamics (MD) simulations have been widely used in shale reservoir research. Using MD simulations, some researchers have investigated the wettability of mineral and organic surfaces.<sup>44–46</sup> Chen et al.<sup>47</sup> investigated the shale gas adsorption capacity. Xiong et al.<sup>48–50</sup> investigated the adsorption of polycyclic aromatic compounds on silica surfaces and the synergistic adsorption of polyaromatic compounds. Wang et al.<sup>51</sup> investigated the competitive adsorption of methane and ethane on nanopores under

supercritical conditions. In addition, some researchers used MD simulations to study the characteristics of fluids in clay minerals. Xiong et al.<sup>52</sup> studied the adsorption behavior of methane on kaolinite and investigated the effect of water content on the adsorption of  $\text{CH}_4$ . Zhang et al.<sup>53</sup> studied the effect of dry and wet kaolinite (1–5%) on the adsorption capacity of  $\text{CH}_4$ , and the results were consistent with those of Xiong et al.<sup>52</sup> Leebyn and Evgeniy<sup>54</sup> investigated the adsorption of  $\text{CO}_2$ ,  $\text{CH}_4$ ,  $\text{K}^+$ , and  $\text{H}_2\text{O}$  mixed-phase hybrid systems on the surface of illite and found that water molecules preferentially adsorbed on the clay surface, forming a water film, and limiting the access of  $\text{CO}_2$  and  $\text{CH}_4$  to the adsorption sites. Some researchers have explored the effect of water content on hydrocarbon occurrence under different conditions, and the results are consistent with those of previous studies.<sup>37,44,51,54</sup>

The study of fluids in clay minerals mainly focuses on hydrocarbons. The study of water mainly focuses on the effect of water content on the occurrence of hydrocarbons; the temperature is up to 80 °C and the pressure does not exceed 70 MPa. Studies on the occurrence of liquid water at high temperatures and pressures are lacking.

In this study, MD simulations were used to study the occurrence characteristics of liquid water in kaolinite nanopores under high-temperature (80–120 °C) and high-pressure (70–120 MPa) conditions. The effects of temperature, pressure, and mineralization (anions and cations) on the presence of water in kaolinite nanopores were explored separately to understand the competitive adsorption characteristics of methane and water.

## 2. METHODOLOGY

**2.1. Molecular Models.** In this study, the MD simulation method, which is a computer-implemented simulation experiment at the molecular scale, was applied. This method employs classical mechanics or quantum mechanics methods to obtain the macroscopic properties and fundamental laws of a system by studying the laws of motion of microscopic molecules.<sup>55–57</sup> In this study, all MD simulations were implemented using Gromacs-2019.6. and molecular visualization software using VMD-1.9.3.

This study used the all-atom model, which has the advantage that its simulations of ionic and liquid systems are very close to the actual characterization results (atomic force microscope (AFM), neutron scattering, etc.).<sup>58</sup> In this study, kaolinite, water molecules, methane molecules,  $\text{Ca}^{2+}$  ions, and  $\text{Cl}^-$  ions

were used and their initial configurations are shown in Figure 1. The initial kaolinite cell configuration was obtained from the American Crystal Structure database. The basal area of the kaolinite cell built in the simulation was  $62.594 \text{ \AA} \times 61.848 \text{ \AA}$  ( $X \times Y$ ) with a height ( $Z$ ) of  $19.173 \text{ \AA}$ .

The two exposed planes in the  $Z$ -direction of kaolinite are the hydrophilic surface of hydroxylation and the lipophilic surface of siloxane. During the simulation, to better understand the characteristics of water occurrence in kaolinite, surfaces of different natures were selected on both sides of the pores. A vacuum layer was established in the middle to build a slit-like kaolinite pore structure, and periodic boundaries were added in the  $X-Y$  direction of kaolinite cells to eliminate the surface or boundary effects. The water molecular model adopts SPC/E, which can better simulate the properties of a liquid water system. The methane molecule bond length was  $1.099 \text{ \AA}$  and the bond angle was  $109.471 \text{ \AA}$ .<sup>59</sup>

**2.2. Force Field.** The molecular force field is a set of potential functions that describes the interactions of molecular systems. The accuracy of MD simulations depends on the force field and selection of force parameters.<sup>56,57</sup> In this study, the CLAYFF force field, optimized specifically for clay minerals, was used for kaolinite, and the CHARMM36 force field was used for the internal fluid components. CHARMM36 is a high-precision force field whose parameters are based on high-precision quantum mechanical calculations, and it is a force field that allows atomic-scale simulation studies of condensed systems. The optimization of this force field is more conducive in achieving good agreement with experimental data. It is available for studying systems that include all common inorganic and organic small molecules, polymers, metals, and metal oxides.<sup>60</sup> The potential function of the force field mainly includes bonded and nonbonded interactions. The simulated system describes the interactions between different substances through nonbonding interactions.

The bonded interaction potential energy is expressed as:

$$U_{\text{bonded}} = \nu_{\text{bond length}} + \nu_{\text{bend angle}} + \nu_{\text{torsion}} \quad (1)$$

where  $U_{\text{bonded}}$ : the bonded interaction energy;  $\nu_{\text{bond length}}$ : the two-body potential energy resulting from bond length deformation;  $\nu_{\text{bend angle}}$ : the three-body potential energy resulting from the angular vibrational motion between the three atoms;  $\nu_{\text{torsion}}$ : the potential energy resulting from the rotation around the bond.

The nonbonded interaction potential energy is expressed as the sum of the Lennard-Jones<sup>61</sup> and Coulomb's electrostatic potentials:<sup>62</sup>

$$\begin{aligned} U_{\text{non-bonded}} &= \nu_{\text{LJ}} + \nu_{\text{C}} = \sum_{i,j(i < j)} 4\epsilon_{ij} \left( \left( \frac{\delta_{ij}}{r_{ij}} \right)^{12} - \left( \frac{\delta_{ij}}{r_{ij}} \right)^6 \right) \\ &+ \sum_{i,j(i < j)} \frac{1}{4\pi\epsilon_0} \cdot \frac{q_i q_j}{r_{ij}} \end{aligned} \quad (2)$$

where, for each pair of  $ij$  atoms,  $\epsilon$  refers to the potential well depth (i.e., the region around the local minimum of the potential energy);  $\sigma$  is the distance between the pair of atoms where the potential energy is zero;  $r_{ij}$  is the distance between the two ions;  $q_i$  and  $q_j$  are the electrostatic point charges of particles  $i$  and  $j$ , respectively;  $\epsilon_0$  is the dielectric constant in free space.

**2.3. Simulation Details.** Three different systems were established in this simulation: (I) a pure water system, (II) a  $\text{CaCl}_2$  solution system, and (III) a  $\text{H}_2\text{O}-\text{CH}_4$  mixed system. First, an energy minimization calculation of the simulated system was performed using the fastest descent method and a conjugate gradient algorithm to obtain a stable initial configuration by continuously adjusting the positions of the atoms. We then ran an equilibrium simulation of the system; the simulation duration was 5 ns and the simulation step size was 1 fs. The final simulation was performed after the equilibrium of the system was determined by the RMSD (Root Mean Square Deviation which is the sum of the squares of particle displacements followed by the square root, and finally the mean value data under isothermal and isobaric conditions were collected and analyzed).

Systems I and II isothermal and isobaric simulations were carried out under an  $NPT$  ensemble (the total number of particles ( $N$ ), the pressure ( $P$ ), and the temperature ( $T$ ) of the system are conserved): (1) isobaric simulation, with the pressure set at 70 MPa and the temperature controlled at 80–120 °C (simulation at 5 °C intervals); (2) isothermal simulation, with the temperature controlled at 80 °C and the pressure set at 70–120 MPa (simulation at 10 MPa intervals).

For system III, we used the  $NVT$  ensemble (the total number of particles ( $N$ ), the total volume ( $V$ ), and the temperature ( $T$ ) of the system are fixed), and the temperature was controlled at 80–120 °C (simulation at 10 °C intervals), the equilibrium simulation was 5 ns, and the final simulation 5 ns was used for the statistical analysis of the simulation results. During the simulation, the pressures were selected based on the formation pressure statistics of marine shale gas wells in southern China, as shown in Figure 2. Some scholars' studies

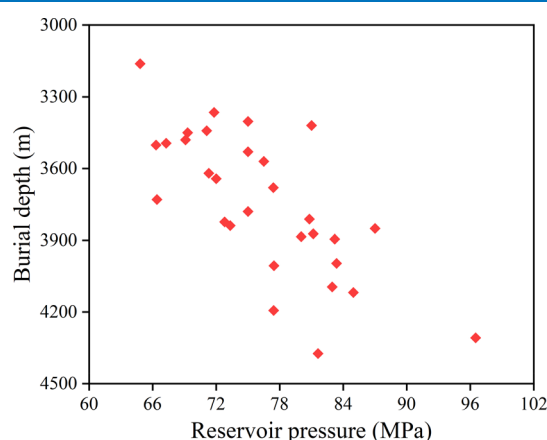


**Figure 2.** Statistical distribution of reservoir pressure in some marine shale gas wells in southern China.

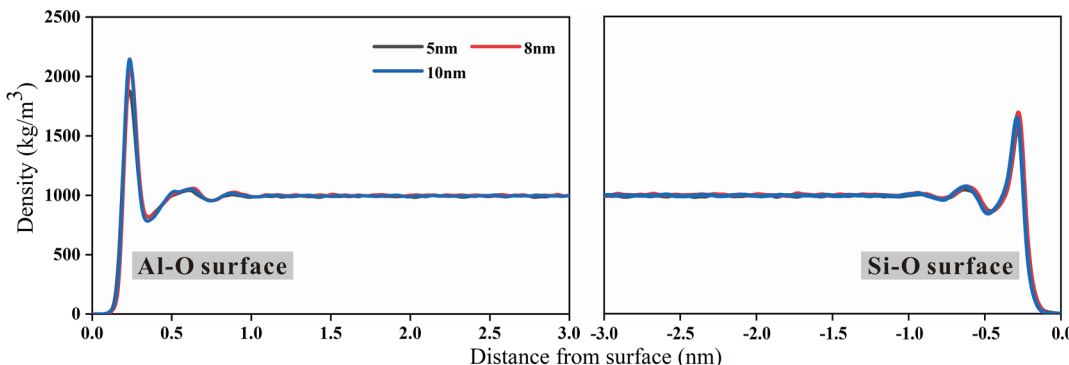
also mentioned that, at present, in southern China marine shale gas wells, the burial depth of the exploited formation section is generally  $>3500 \text{ m}$ , the pressure is generally  $>70 \text{ MPa}$ , and the temperature is generally  $>80 \text{ }^\circ\text{C}$ . The temperature-pressure settings in this paper restore the in situ conditions.<sup>63–65</sup>

### 3. RESULTS AND DISCUSSION

This study focuses on the influence of temperature, pressure, and other factors on the state of water occurrence in different systems. In the simulation process, the authors neglected the

**Table 1.** Statistical Results of Adsorption Parameters of Water with Different Pore Sizes

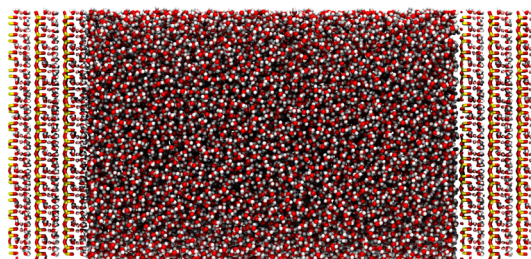
adsorption parameter	adsorption peak	pore diameter			
		5 nm	8 nm	10 nm	
Al–O octahedral surface	adsorption thickness (nm)	main peak	0.2836	0.2842	0.2835
		secondary peak	0.3697	0.3797	0.3780
	adsorption capacity per unit area (mg/m <sup>2</sup> )	main peak	0.6273	0.6309	0.6312
		secondary peak	0.6373	0.6309	0.6382
	average mass density of adsorbed phase (kg/m <sup>3</sup> )	main peak	0.7918	0.7924	0.7916
		secondary peak	0.9689	0.9640	0.9595
Si–O tetrahedral surface	absorption phase mass ratio (%)		13.0500	8.3900	6.7309
	adsorption thickness (nm)	main peak	0.4254	0.4264	0.4253
		secondary peak	0.3276	0.3285	0.3315
	adsorption capacity per unit area (mg/m <sup>2</sup> )	main peak	0.6545	0.6569	0.6543
		secondary peak	0.7312	0.7346	0.7275
	average mass density of adsorbed phase (kg/m <sup>3</sup> )	main peak	0.6920	0.6885	0.6926
absorption phase mass ratio (%)		secondary peak	0.9776	0.9758	0.9827
	total adsorption phase mass ratio (%)		12.5293	8.1698	6.8630
			25.5793	16.5598	13.5939

**Figure 3.** Adsorption density curves of water at different pore sizes.

unity of the slit pore diameter between different systems to avoid doubts regarding this. Therefore, before discussing the results, it is important to first confirm whether there is an effect of pore size on the water occurrence state. By performing a simulation of the slit pores of the pure water system with widths of 5, 8, and 10 nm, we analyzed the statistical adsorption data, and the results obtained are described in the text that follows.

Fortunately, changes in pore size have little effect on the state of water occurrence. Adsorption parameters (Table 1), such as adsorption thickness, adsorption capacity per unit area, and the average mass density of the waterbed phase, were only slightly different. The following conclusions can also be drawn from Figure 3 (in the following illustrations of the same type, the Al–O surface is on the left, and the Si–O surface is on the right). If statistical errors had been excluded, the results would have been the same. Therefore, the change in the pore size did not change the related water adsorption parameters. The change in the absorption phase mass ratio occurred because the larger the pore diameter, the more free water was distributed within it, resulting in a reduction in the absorption phase proportion.

**3.1. Occurrence of the Pure Water System.** To study the effects of temperature and pressure on the occurrence of water in kaolinite, isothermal and isobaric simulations were conducted in 10 nm slit pores. Then, the distribution characteristics of the water molecular density and RMSD (Figures 4 and 5).

**Figure 4.** Molecular conformation after the simulation equilibrium.

After the simulation, the RMSD of the H<sub>2</sub>O molecules gradually stabilized with increasing simulation time, that is, the system reached an equilibrium state. The RMSD is often used in trajectory analysis to determine whether the system is in equilibrium. Figure 5a shows that the RMSD of H<sub>2</sub>O decreased with an increase in pressure. In contrast to the pressure, an increase in temperature caused a gradual increase in the RMSD of H<sub>2</sub>O, and the curve of the isobaric simulation showed a larger variation than that of the isothermal simulation (Figure 5b). This phenomenon is thought to be due to an increase in pressure, which leads to a decrease in the motility of H<sub>2</sub>O molecules, while an increase in temperature leads to an increase in the motility of H<sub>2</sub>O molecules.

Changes in molecular motility are important causes of adsorption and desorption on mineral surfaces. Increased motility increases the probability of free water molecules

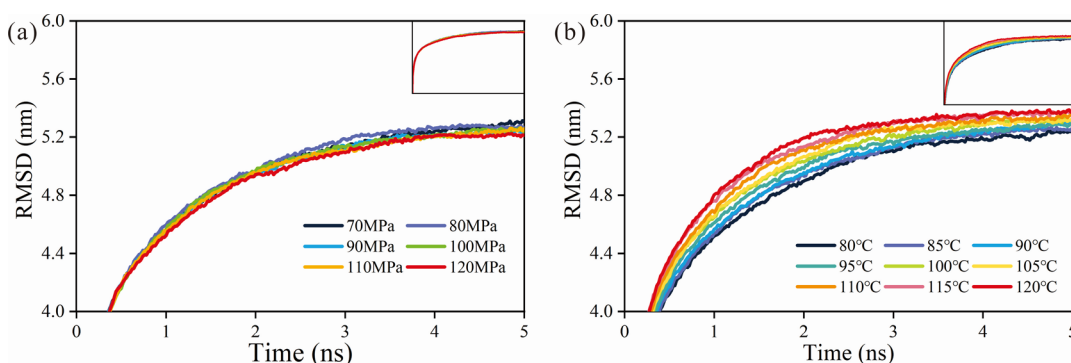


**Figure 5.** RMSD plots of  $\text{H}_2\text{O}$  molecules in isothermal (a) and isobaric (b) simulations.

hitting the adsorbed water molecules, which leads to the desorption of water molecules with weak interactions with the mineral surface and reduces the adsorption amount.

Corresponding to the density distribution of the water molecules (Figure 6), the change in pressure had no effect on

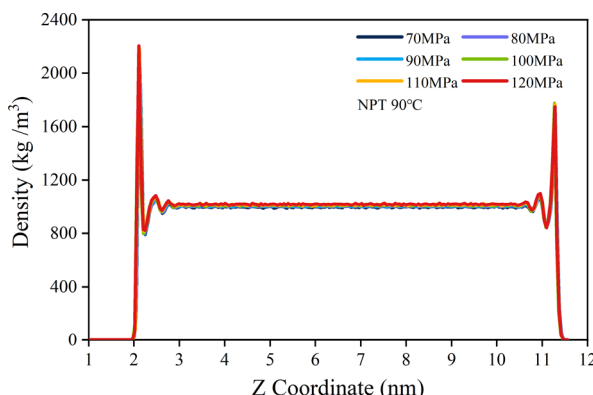


**Figure 6.** Density distribution of  $\text{H}_2\text{O}$  molecules in the isothermal simulation.

the adsorption capacity of the water molecules on the kaolinite surface. The mass density of water molecules at the center of kaolinite slit pores (approximately 2.8–10.8 nm from the Al–O octahedron) was essentially kept constant at  $1000 \text{ kg/m}^3$ , which is the density of water under standard conditions. The adsorption peaks near both sides of the kaolinite surface were considered adsorption states.

Isothermal simulation results (Figure 6): (1) The adsorption thickness is essentially the same: (a) main peak 0.28 nm and secondary peak 0.37 nm on the Al–O octahedron surface; (b) main peak 0.42 nm and secondary peak 0.33 nm on the Si–O tetrahedron surface. (2) The highest value of the adsorption phase density curve was  $2.09 \text{ g/cm}^3$ , and the total adsorption phase mass ratio was approximately 13.31%.

The isobaric simulation results are shown in Table 2 and Figure 7, which indicate that temperature has a greater effect on the adsorption of water on kaolinite surfaces than pressure. In addition to the difference in adsorption owing to the motility of molecules, there was also a difference in the adsorption of water molecules on surfaces of different nature, which is due to the hydrogen bond interaction of water with the Al–O octahedral surface and the van der Waals interaction with the Si–O tetrahedral surface, where the hydrogen bond interaction is stronger than the van der Waals interaction forces.

In addition, the simulation also investigated the water adsorption differences on kaolinite surfaces under normal temperature and pressure conditions and high temperature and pressure conditions. A comparison of the adsorption density distribution of water at  $25^\circ\text{C}$  (0.1 MPa) with that at  $80^\circ\text{C}$  (70 MPa) (Figure 8) showed that the adsorption peaks on the surface of the Si–O tetrahedra overlapped, and the adsorption peaks at room temperature were relatively higher; however, the differences were small, which was consistent with the effect of temperature on the adsorption of water on mineral surfaces. Therefore, it is considered that normal temperature and pressure can be used to study the occurrence of water in shale.

### 3.2. Occurrence of Water in the $\text{CaCl}_2$ Solution System.

The pore water of marine shale in southern China is mainly the  $\text{CaCl}_2$  type, followed by the  $\text{NaHCO}_3$  type.<sup>66</sup> Some scholars believe that the first stage mainly drains the fracturing fluid and the later stage gradually excludes the formation water.<sup>13</sup> Thus, the adsorption of  $\text{CaCl}_2$  salt solution on kaolinite was simulated to investigate the difference between the occurrence of formation water and pure water in kaolinite.

A 5 nm kaolinite slit pore was established, in which  $100 \text{ Ca}^{2+}$  and  $200 \text{ Cl}^-$  were added (Figure 9a), corresponding to a mineralization of  $9130.6 \text{ mg/L}$ . After the simulation, the density distribution characteristics of the water molecules  $\text{Ca}^{2+}$  and  $\text{Cl}^-$  were collected and analyzed.

The distribution of water molecules is the same as above, and the thickness of  $\text{H}_2\text{O}$  adsorption on the Al–O octahedron is 0.28 nm for the main peak and 0.37 nm for the secondary peak; the adsorption on the Si–O tetrahedron surface is 0.42 nm for the main peak and 0.33 nm for the secondary peak (Figure 9b). The total adsorption phase mass ratio of  $\text{H}_2\text{O}$  in this system was 19.8%. Anions and cations in the system aggregate on different surfaces.  $\text{Cl}^-$  was partially adsorbed and aggregated on the surface of the Al–O octahedron, while  $\text{Ca}^{2+}$  was partially adsorbed and aggregated on the surface of the Si–O tetrahedron (Figure 9c,d).

A comparison of the density curves of water at different temperatures and pressures (Figure 10a,b) showed that the change of pressure in this system did not cause any change in water adsorption on the kaolinite surface. However, an increase in temperature decreased the water adsorption on the Si–O surface and did not affect the Al–O surface. It is consistent with the change in the pure water system.

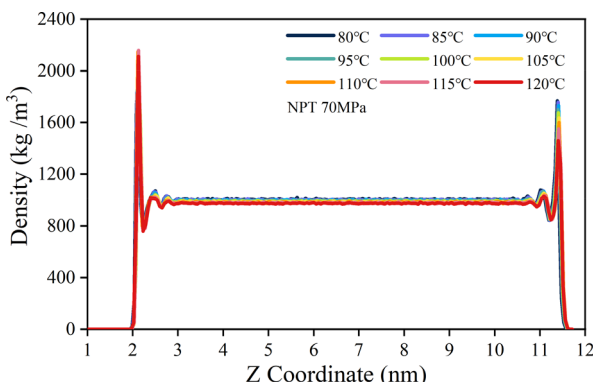
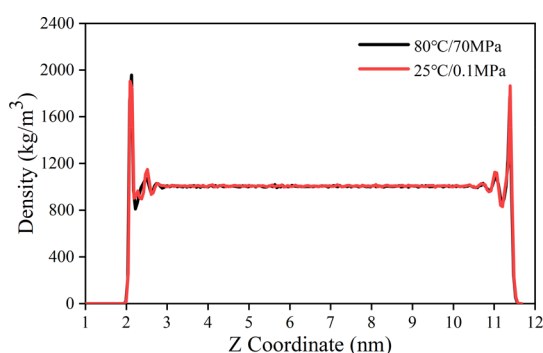
A comparative analysis of the mass density curve of water in the pure water system and the mass density curve of water in the  $\text{CaCl}_2$  solution was carried out. The results showed that the adsorption mass density of the Si–O tetrahedral surface of

**Table 2.** Statistics of Adsorption Parameters for Isobaric Simulation Results at 80–120 °C (70 MPa)

temperature	adsorption thickness (nm)		adsorption capacity per unit area (mg/m <sup>2</sup> )		absorption phase mass ratio (%)
	main peak	secondary peak	main peak	secondary peak	
80 °C	0.28	0.37	0.63	0.64	6.67
85 °C	0.28	0.37	0.63	0.64	6.70
90 °C	0.28	0.37	0.63	0.64	6.73
95 °C	0.28	0.37	0.63	0.64	6.75
100 °C	0.28	0.37	0.65	0.64	6.74
105 °C	0.28	0.37	0.65	0.64	6.75
110 °C	0.28	0.37	0.65	0.64	6.76
115 °C	0.28	0.37	0.65	0.64	6.73
120 °C	0.28	0.37	0.65	0.64	6.70

temperature	adsorption thickness (nm)		adsorption capacity per unit area (mg/m <sup>2</sup> )		absorption phase mass ratio (%)	total adsorption phase mass ratio (%)
	main peak	secondary peak	main peak	secondary peak		
80 °C	0.42	0.33	0.653	0.737	6.84	13.51
85 °C	0.42	0.33	0.653	0.733	6.85	13.55
90 °C	0.42	0.33	0.649	0.727	6.58	13.31
95 °C	0.42	0.33	0.648	0.727	6.56	13.31
100 °C	0.42	0.33	0.648	0.724	6.54	13.28
105 °C	0.42	0.33	0.648	0.72	6.52	13.27
110 °C	0.42	0.33	0.648	0.72	6.48	13.24
115 °C	0.42	0.33	0.647	0.718	6.45	13.18
120 °C	0.42	0.33	0.47	0.712	6.23	12.93

**Figure 7.** Density distribution of H<sub>2</sub>O molecules in the isobaric calculation.**Figure 8.** Density distribution of H<sub>2</sub>O molecules at 25 °C (0.1 MPa) and 80 °C (70 MPa).

both overlapped, but the adsorption of pure water on the Al–O octahedral surface was slightly greater than that of water in the salt solution.

It is thought that the Cl<sup>−</sup> content in the salt solution is twice that of Ca<sup>2+</sup>, and thus occupies more adsorption sites on the Al–O octahedral surface, resulting in slightly lower adsorption than that of pure water (Figure 10c,d). Therefore, solutions with a certain degree of mineralization should be used in the study of subsurface water conditions.

**3.3. Occurrence of the H<sub>2</sub>O–CH<sub>4</sub> System.** The occurrence in 8 and 5 nm kaolinite slit pores simulated under the NVT system synthesis was examined. A H<sub>2</sub>O:CH<sub>4</sub> ratio of 3:1 within a pore with a pore size of 8 nm corresponded to a gas saturation of 25%, and a ratio of H<sub>2</sub>O:CH<sub>4</sub> of 11.6:1 in pores with a pore size of 5 nm corresponded to a gas saturation of 8.6%. The random distribution of water and methane molecules under initial conditions (Figure 11a) was simulated at a temperature controlled at 80–120 °C (simulation at 10 °C intervals).

After the simulation reached equilibrium, most methane molecules were aggregated and adsorbed on the surface of the Si–O tetrahedron in the system with a gas saturation of 25%, but only a small number of methane molecules were free in water owing to gas–solid interactions and hydrogen bond interactions between water molecules (Figure 11b). Water molecules still underwent two-layer adsorption on both surfaces. However, owing to the presence of methane molecules, the adsorption peak of water on the Si–O tetrahedral surface and the density of free water were significantly reduced, which is complementary to methane.

As the Al–O octahedral surface of kaolinite is hydrophilic, only a small degree of CH<sub>4</sub> adsorption occurs. As can be seen in Figure 11b,c, its adsorption position is consistent with that of the second layer of adsorbed water (circled by the black dotted line in the figure). Also, in Figure 12, by zooming in on the kaolinite Al–O surface, it can be seen that CH<sub>4</sub> is not in direct contact with the Al–O surface and strong hydrogen bonding interactions occur between the Al–O surface and

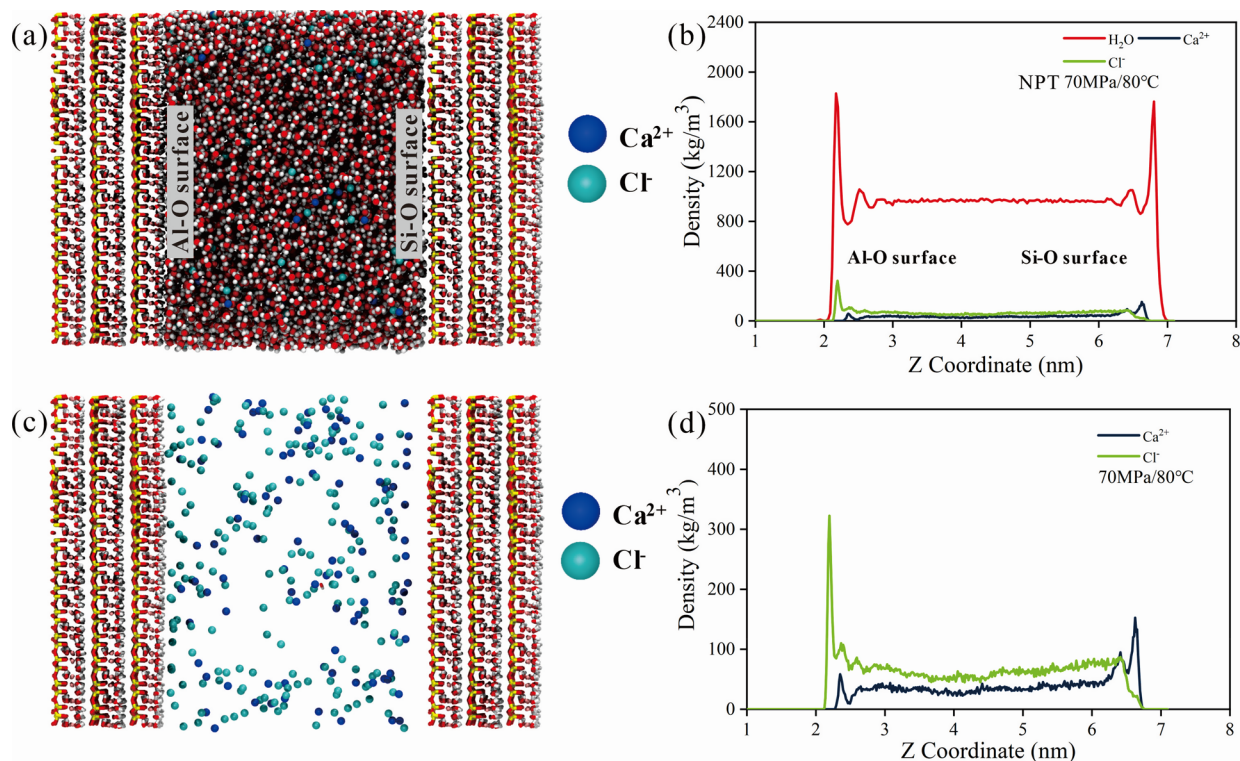


**Figure 9.** (a) Molecular conformation diagram after the simulated equilibrium of  $\text{CaCl}_2$  solution; (b) ion density distribution diagram of water at 70 MPa/80 °C; (c) particle distribution diagram after simulated equilibrium; (d) ion density distribution diagram at 70 MPa/80 °C (enlarged).

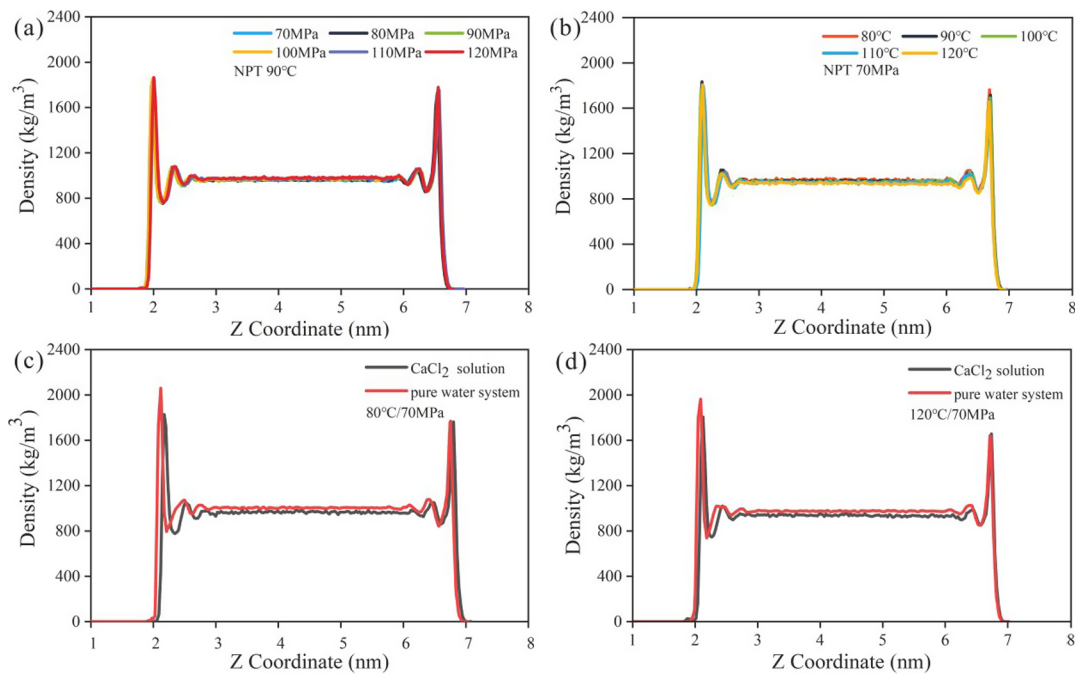


**Figure 10.** (a) Density distribution of water in a  $\text{CaCl}_2$  solution at isothermal conditions. (b) Density distribution of water at isobaric conditions. (c, d) Adsorption density distribution of water in pure water and a  $\text{CaCl}_2$  solution at 80 °C/70 MPa and 120 °C/70 MPa.

water, and methane can only compete in small amounts with the second layer of adsorbed water for adsorption sites. Therefore, it is believed that the adsorption occurs between  $\text{CH}_4$  and the first layer of adsorbed water molecules, that is, solid–liquid–gas interactions.

The adsorption of  $\text{H}_2\text{O}$  in the mixed system occurs mainly on the Al–O octahedral surface, while the adsorption on the

Si–O tetrahedral surface is significantly reduced owing to lipophilicity, with only 21% of the adsorption on the Al–O octahedral surface (Figure 13a). The system corresponding to a gas saturation of 8.6% also exhibited these characteristics. The interaction between the adsorbing molecules and the kaolinite surface is shown in Figure 12.  $\text{H}_2\text{O}$  interacts with the Al–O octahedral surface of kaolinite by hydrogen bonding,

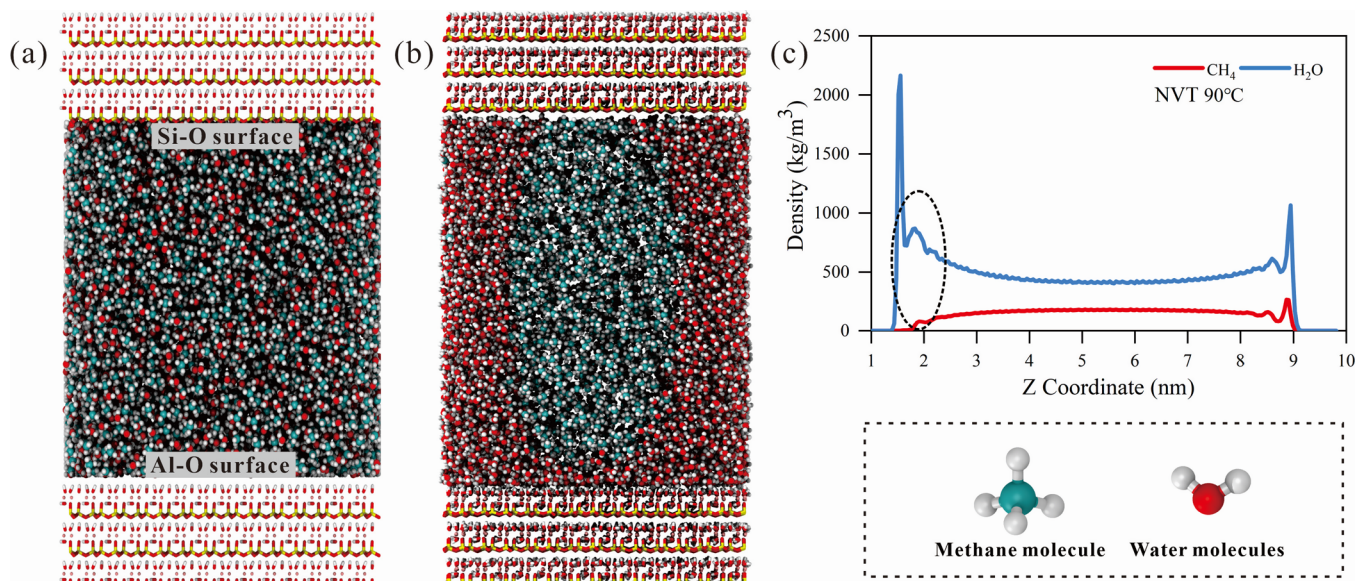


**Figure 11.** (a) Initial state molecular configuration; (b) molecular configuration after the simulated equilibrium; (c) density profile of water and methane at 90 °C.

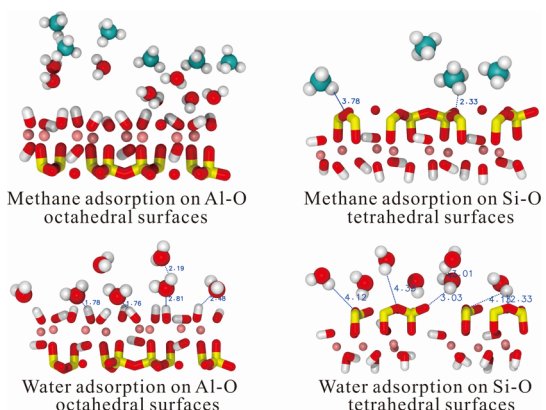
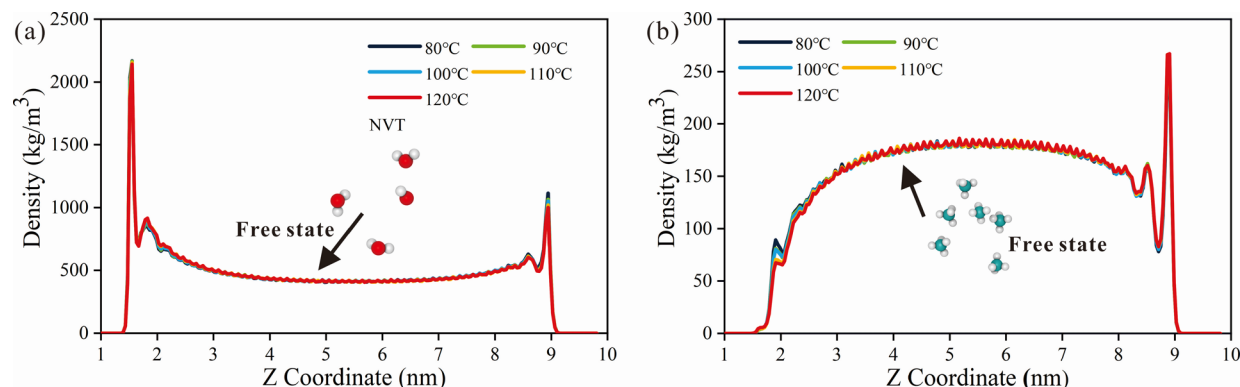


**Figure 12.** Adsorption diagram of methane and water on Al–O octahedral and Si–O tetrahedral surfaces.

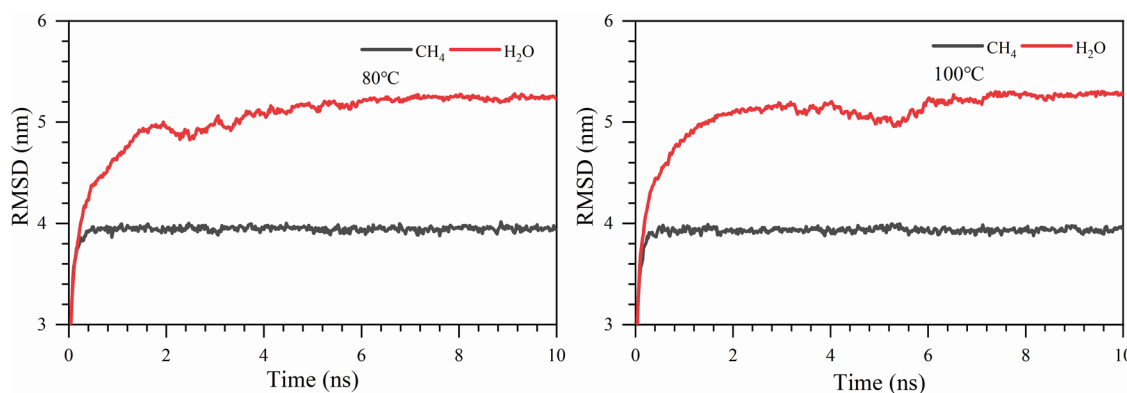
and CH<sub>4</sub> interacts with H<sub>2</sub>O, which is adsorbed on the Al–O octahedral surface of kaolinite, via van der Waals interactions; H<sub>2</sub>O and CH<sub>4</sub> interact with the Si–O tetrahedral surface of kaolinite via van der Waals interactions (hydrogen bonding interactions > van der Waals interactions).

Next, the effect of temperature on the occurrence of fluids in the system is discussed. As the temperature increased, the peak of the small-amplitude adsorption layer of CH<sub>4</sub> on the Al–O octahedral surface gradually decreased owing to the elevated second adsorption layer of water molecules, which decreased the amount of methane adsorbed. The peak of the adsorption layer of CH<sub>4</sub> on the Si–O tetrahedral surface gradually increased, probably because the adsorption peak of water molecules on the Si–O tetrahedral surface decreased with increasing temperature, providing more adsorption sites for CH<sub>4</sub> molecules (Figure 13b).

Unlike CH<sub>4</sub>, the adsorption of H<sub>2</sub>O on both kaolinite surfaces decreased with increasing temperature, but the adsorption on the Al–O octahedral surface was less affected by temperature. The RMSD of H<sub>2</sub>O was much larger and more mobile than that of the CH<sub>4</sub> molecule (Figure 14), and therefore more likely to collide and desorb as the temperature increased. This phenomenon is also related to the forces exerted on the H<sub>2</sub>O molecules, which produce hydrogen bonding with the Al–O octahedral surface and are more strongly resistant to desorption than the van der Waals interactions produced by the H<sub>2</sub>O molecules with the Si–O tetrahedra, so the temperature has less influence on the



**Figure 13.** CH<sub>4</sub>–H<sub>2</sub>O mixed system with 25% gas saturation; (a) water density fraction graph; (b) methane density fraction graph.

Figure 14. RMSD of  $\text{CH}_4$  versus  $\text{H}_2\text{O}$ .**Table 3. Statistics of Simulation Results for the  $\text{CH}_4-\text{H}_2\text{O}$  Mixed System with 25% Gas Saturation**

temperature	$\text{H}_2\text{O}$								
	adsorption thickness (nm)				adsorption capacity per unit area ( $\text{mg}/\text{m}^2$ )				
	Al-O surface		Si-O surface		Al-O	Si-O	absorption phase mass ratio (%)		
80 °C	main peak	0.28	secondary peak	0.27	0.3	0.31	0.66	0.43	25.4
90 °C	main peak	0.28	secondary peak	0.27	0.3	0.31	0.66	0.43	25.4
100 °C	main peak	0.28	secondary peak	0.27	0.3	0.31	0.66	0.43	25.4
110 °C	main peak	0.28	secondary peak	0.27	0.3	0.31	0.66	0.43	25.4
120 °C	main peak	0.28	secondary peak	0.27	0.3	0.31	0.66	0.43	25.4

temperature	$\text{CH}_4$					
	adsorption thickness (nm)			adsorption capacity per unit area ( $\text{mg}/\text{m}^2$ )		
	Al-O surface		Si-O surface	absorption phase mass ratio (%)		
80 °C	main peak	0.24	0.3	0.21	0.082	9.22
90 °C	main peak	0.24	0.3	0.21	0.083	9.35
100 °C	main peak	0.24	0.3	0.21	0.082	9.26
110 °C	main peak	0.24	0.3	0.21	0.082	9.20
120 °C	main peak	0.24	0.3	0.21	0.082	9.21

adsorption on the Al–O octahedral surface (Figure 14); the specific adsorption data characteristics are shown in Table 3.

The adsorption of  $\text{H}_2\text{O}$  in the slit pore in the  $\text{CH}_4-\text{H}_2\text{O}$  mixed system containing 8.6% gas saturation (Figure 15a,b), according to the statistical adsorption values and density curves, can be obtained so that the adsorption peak of  $\text{H}_2\text{O}$  in the Al–O octahedron does not change with the increase of temperature and the adsorption peak on the surface of Si–O tetrahedron is constant at 80–100 °C and slightly decreases at >100 °C (Figure 15c). In terms of the adsorption of  $\text{CH}_4$  in the slit pore,  $\text{CH}_4$  adsorption occurred only on the surface of the Si–O tetrahedra and increased with increasing temperature (Figure 15d).

$\text{H}_2\text{O}-\text{CH}_4$  two-phase system: (a) The effect of the temperature change on the water was consistent with that in the pure water system, where the adsorption of  $\text{CH}_4$  mainly occurred on the Si–O tetrahedral surface. As the temperature increased, the adsorption of water decreased, providing more adsorption sites for the adsorption of  $\text{CH}_4$ , so the amount of  $\text{CH}_4$  adsorption increased. (b) When the  $\text{CH}_4$  content was low, it only aggregated on the Si–O tetrahedral surface, whereas when the methane content was high, adsorption could occur on the first adsorbed  $\text{H}_2\text{O}$  layer on the Al–O octahedral surface, that is, competing with the second adsorbed  $\text{H}_2\text{O}$  layer.

#### 4. CONCLUSIONS

- (1) In this study, molecular simulations revealed that the occurrence characteristics of water in kaolinite were as follows: the Al–O octahedral surface exhibited strong hydrophilicity owing to hydrogen bonding interactions between hydroxylation and water, while the Si–O tetrahedral surface exhibited van der Waals interactions with water, which are relatively weak and vary greatly when influenced by external conditions.
- (2) The effects of temperature, pressure, and ions on the occurrence of water are summarized as follows: (a) pressure had no effect on the occurrence of water in kaolinite; (b) the adsorption on the surface of the Al–O octahedron remained unchanged when the temperature increased, while the adsorption on the surface of the Si–O tetrahedron decreased slightly with an increase in temperature; (c) the presence of ions caused the adsorption of water on the surface of the Al–O octahedron to decrease significantly. Therefore, a solution with a certain degree of mineralization should be considered when studying water formation conditions.
- (3) The density distribution curves of water at room temperature and pressure were compared with those at

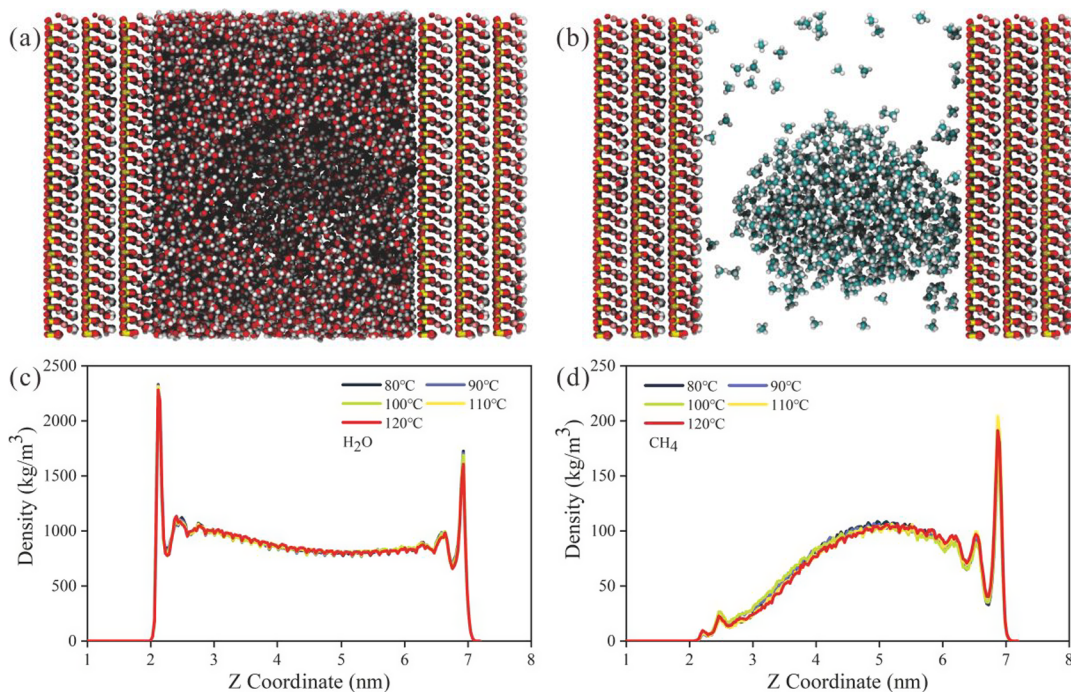


**Figure 15.** Mixed  $\text{CH}_4\text{--H}_2\text{O}$  system with gas saturation of 8.6%. (a) Water distribution configuration, (b) methane distribution configuration, (c) water density fraction profile, (d) and methane density fraction profile.

high temperature and pressure and were found to overlap, indicating that the study of the occurrence of water in clay minerals could be carried out directly at room temperature and pressure.

- (4) In the  $\text{H}_2\text{O}\text{--CH}_4$  two-phase system, (a)  $\text{CH}_4$  molecules gathered into clusters and adsorption occurred on the Si–O tetrahedral surface; when the  $\text{CH}_4$  content was high, adsorption occurred on the Al–O octahedral surface, but not directly with the solid surface, but with the first layer of adsorbed water molecules by van der Waals interactions (solid–liquid–gas interactions); (b) the increase in temperature reduced the adsorption of water, thus providing more adsorption sites for the adsorption of  $\text{CH}_4$ , which increased the amount of  $\text{CH}_4$  adsorption.

## AUTHOR INFORMATION

### Corresponding Author

**Junqian Li** – School of Geosciences and Shandong Provincial Key Laboratory of Deep Oil & Gas, China University of Petroleum (East China), Qingdao 266580, China; [orcid.org/0009-0004-9160-2628](https://orcid.org/0009-0004-9160-2628); Email: [lijunqian@upc.edu.cn](mailto:lijunqian@upc.edu.cn)

### Authors

**Zhiyan Zhou** – School of Geosciences and Shandong Provincial Key Laboratory of Deep Oil & Gas, China University of Petroleum (East China), Qingdao 266580, China

**Zhaojing Song** – School of Geosciences and Shandong Provincial Key Laboratory of Deep Oil & Gas, China University of Petroleum (East China), Qingdao 266580, China

**Rixin Zhao** – School of Geosciences and Shandong Provincial Key Laboratory of Deep Oil & Gas, China University of Petroleum (East China), Qingdao 266580, China

Complete contact information is available at:  
<https://pubs.acs.org/10.1021/acsomega.3c01640>

### Notes

The authors declare no competing financial interest.  
The data used to support the findings of this study are included within the article.

### ACKNOWLEDGMENTS

This study was financially supported by the National Natural Science Foundation of China (41972123).

### REFERENCES

- Zou, C.; Yang, Z.; Dong, D.; Zhao, Q.; Chen, Z.; Feng, Y.; Li, J.; Wang, X. Formation, Distribution and Prospect of Unconventional Hydrocarbons in Source Rock Strata in China. *Earth Sci.* **2022**, *47*, 1517–1533.
- Zhao, W.; Jia, A.; Wei, Y.; Wang, J.; Zhu, H. Progress in shale gas exploration in China and Prospects for future development. *China Pet. Explor.* **2020**, *25*, 31–44.
- Li, G.; Zhu, R. Progress, challenges and key issues in the unconventional oil and gas development of CNPC. *China Pet. Explor.* **2020**, *25*, 1–13.
- Sun, J.; Su, H.; Guo, N.; Wang, D.; Zeng, X.; Yuan, W.; Feng, M.; Yan, W.; Zhou, X. Determination method of biogenic silicon and its application in the fracturing ability evaluation of shale gas reservoir. *Acta Petrol. Sin.* **2022**, *43*, 548–557.
- Long, S.; Feng, D.; Li, F.; Du, W. Prospect of the deep marine shale gas exploration and development in the Sichuan Basin. *Nat. Gas Geosci.* **2018**, *3*, 443–489.
- Wang, Z.; Jiang, Y.; Fu, Y.; Lei, Z.; Xu, C.; Yuan, J.; Wen, R.; Wang, Z.; Gu, Y.; Yin, X. Characterization of Pore Structure and Heterogeneity of Shale Reservoir from Wufeng Formation-Sublayers Long-11 in Western Chongqing Based on Nuclear Magnetic Resonance. *Earth Sci.* **2022**, *47*, 490–504.
- Chen, S.; Zhu, Y.; Wang, H.; Liu, H.; Wei, W.; Fang, J. Characteristics and significance of mineral composition of Lower

- Silurian Longmaxi Formation shale gas reservoirs in the southern margin of Sichuan Basin. *Acta Petrol. Sin.* **2011**, *32*, 775–782.
- (8) Guo, X.; Tenger, B.; Wei, X.; Yu, L.; Lu, X.; Sun, L.; Wei, F. Occurrence mechanism and exploration potential of deep marine shale gas in Sichuan Basin. *Acta Petrol. Sin.* **2022**, *43*, 453–468.
- (9) Guo, X.; Hu, D.; Li, Y.; Wei, Z.; Wei, X.; Liu, Z. Geological factors controlling shale gas enrichment and high production in Fuling shale gas field. *Pet. Explor. Dev.* **2017**, *44*, 513–523.
- (10) Li, Y.; Li, X.; Wang, Y.; Yu, Q. Effects of composition and pore structure on the reservoir gas capacity of Carboniferous shale from Qaidam Basin, China. *Mar. Pet. Geol.* **2015**, *62*, 44–57.
- (11) Fang, C.; Huang, Z.; Wang, Q.; Zheng, D.; Liu, H. Cause and significance of the ultra-low water saturation in gas-enriched shale reservoir. *Nat. Gas Geosci.* **2014**, *25*, 471–476.
- (12) Li, J.; Li, X.; Wang, X.; Li, Y.; Shi, J.; Feng, D.; Bai, Y.; Xu, M. A quantitative model to determine water-saturation distribution characteristics inside shale inorganic pores. *Acta Petrol. Sin.* **2016**, *37*, 903–913.
- (13) Ghanbari, E.; Dehghanpour, H. The fate of fracturing water: A field and simulation study. *Fuel* **2016**, *163*, 282–294.
- (14) Zeng, F.; Zhang, Q.; Guo, J.; Meng, Y.; Shao, X.; Zheng, Y. Capillary imbibition of confined water in nanopores. *Capillarity* **2020**, *3*, 8–15.
- (15) Wang, K.; Ye, B.; Li, K.; Tan, H.; Yong, S. Spontaneous imbibition model for micro–nano–scale pores in shale gas reservoirs considering gas–water interaction. *J. Pet. Sci. Eng.* **2022**, *209*, No. 109893.
- (16) Li, J.; Lu, S.; Zhang, P.; Cai, J.; Li, W.; Wang, S.; Feng, W. Estimation of gas-in-place content in coal and shale reservoirs: A process analysis method and its preliminary application. *Fuel* **2020**, *259*, No. 116266.
- (17) Liu, H.; Wang, H. Ultra-low water saturation characteristics and the identification of over-pressured play fairways of marine shales in south China. *Nat. Gas Ind.* **2013**, *33*, 140–144.
- (18) Li, J.; Wang, S.; Lu, S.; Zhang, P.; Cai, J.; Zhao, J.; Li, W. Microdistribution and mobility of water in gas shale: A theoretical and experimental study. *Mar. Pet. Geol.* **2019**, *102*, 496–507.
- (19) Gasparik, M.; Bertier, P.; Gensterblum, Y.; Ghanizadeh, A.; Krooss, B.; Littke, R. Geological controls on the methane storage capacity in organic-rich shales. *Int. J. Coal Geol.* **2014**, *123*, 34–51.
- (20) Ross, D.; Bustin, R. The importance of shale composition and pore structure upon gas storage potential of shale gas reservoirs. *Mar. Pet. Geol.* **2009**, *26*, 916–927.
- (21) Han, W.; Li, A.; Memon, A.; Ma, M. Synergetic Effect of Water, Temperature, and Pressure on Methane Adsorption in Shale Gas Reservoirs. *ACS Omega* **2021**, *6*, 2215–2229.
- (22) Dong, F.; Li, X.; Zhao, C.; Li, J.; Liu, Q.; He, M.; Zhao, W.; Qin, J. The Role of Adsorbed Water on Pore Structure Characteristics and Methane Adsorption of Shale Clay. C. SPE Trinidad and Tobago Section Energy Resources Conference. Day 2 Tue June 26, 2018.
- (23) Dong, F.; Li, X.; Wang, X.; Li, J.; Sun, F.; Sun, Z.; Zhang, T.; Li, P.; Chen, Y.; Zhang, X. Water adsorption and its impact on the pore structure characteristics of shale clay. *Appl. Clay Sci.* **2018**, *155*, 126–138.
- (24) Li, J.; Li, B.; Gao, Z. Water Vapor Adsorption Behavior in Shale Under Different Temperatures and Pore Structures. *Nat. Resour. Res.* **2021**, *30*, 2789–2805.
- (25) Shen, W.; Li, X.; Cihan, A.; Lu, X.; Liu, X. Experimental and numerical simulation of water adsorption and diffusion in shale gas reservoir rocks. *Adv. Geo-Energy Res.* **2019**, *3*, 165–174.
- (26) Tang, X.; Zhang, T.; Zhang, J.; Sun, X.; Wu, C.; Jin, Z. Effects of pore fluids on methane sorption in the Lower Bakken Shales, Williston Basin, USA. *Fuel* **2020**, *282*, No. 118457.
- (27) Ji, L.; Zhang, T.; Milliken, K. L.; Qu, J.; Zhang, X. Experimental investigation of main controls to methane adsorption in clay-rich rocks. *Appl. Geochem.* **2012**, *27*, 2533–2545.
- (28) Yang, R.; Jia, A.; Hu, Q.; Guo, X.; Sun, M. Particle Size Effect on Water Vapor Sorption Measurement of Organic Shale: One Example from Dongyuemiao Member of Lower Jurassic Ziliujing Formation in Jiannan Area of China. *Adv. Geo-Energy Res.* **2020**, *4*, 207–218.
- (29) Helmenstine, T. "Phases of Matter and Phase Diagrams." ThoughtCo, Apr. 5, 2023, thoughtco.com/phases-of-matter-with-diagrams-608362.
- (30) Stillinger, F. H. Theoretical approaches to the intermolecular nature of water. *Philos. Trans. R. Soc. Lond. B Biol. Sci.* **1977**, *278*, 97–112.
- (31) Merkel, A.; Fink, R.; Little, R. The role of pre-adsorbed water on methane sorption capacity of Bossier and Haynesville shales. *Int. J. Coal Geol.* **2015**, *147–148*, 1–8.
- (32) Li, J.; Li, X.; Wang, X.; Li, Y.; Wu, K.; Shi, J.; Yang, L.; Feng, D.; Zhang, T.; Yu, P. Water distribution characteristic and effect on methane adsorption capacity in shale clay. *Int. J. Coal Geol.* **2016**, *159*, 135–154.
- (33) Wu, K.; Chen, Z.; Li, J.; Li, X.; Xu, J.; Dong, X. Wettability effect on nanoconfined water flow. *PNAS* **2017**, *114*, 3358–3363.
- (34) Gasparik, M.; Ghanizadeh, A.; Bertier, P.; Gensterblum, Y.; Bouw, S.; Krooss, B. M. High-pressure methane sorption isotherms of black shales from the Netherlands. *Energy Fuels* **2012**, *26*, 4995–5004.
- (35) Hao, F.; Zou, H.; Lu, Y. Mechanisms of shale gas storage: Implications for shale gas exploration in China. *AAPG Bull.* **2013**, *97*, 1325–1346.
- (36) Schettler, P.; Parmoly, C. The measurement of gas desorption isotherms for Devonian shale. *GRI Devonian Gas Shale Technol. Rev.* **1990**, *7*, 4–9.
- (37) Liu, D.; Yuan, P.; Liu, H.; Li, T.; Tan, D.; Yuan, W.; He, H. High-pressure adsorption of methane on montmorillonite, kaolinite and illite. *Appl. Clay Sci.* **2013**, *85*, 25–30.
- (38) Zolfaghari, A.; Dehghanpour, H.; Holyk, J. Water sorption behaviour of gas shales: I. Role of clays. *Int. J. Coal Geol.* **2017**, *179*, 130–138.
- (39) Wang, C.-C.; Juang, L.-C.; Lee, C.-K.; Hsu, T.-C.; Lee, J.-F.; Chao, H.-P. Effects of exchanged surfactant cations on the pore structure and adsorption characteristics of montmorillonite. *J. Colloid Interface Sci.* **2004**, *280*, 27–35.
- (40) Fan, E.; Tang, S.; Zhang, C.; Guo, Q.; Sun, C. Methane sorption capacity of organics and clays in high-over matured shale-gas systems. *Energy Explor. Exploit.* **2014**, *32*, 927–942.
- (41) Benazzouz, B. K.; Zaoui, A.; Belonoshko, A. B. Determination of the melting temperature of kaolinite by means of the Z-method. *Am. Mineral.* **2013**, *98*, 1881–1885.
- (42) Chi, Q.; Zhen, R.; Wang, X.; Yang, K.; Jiang, Y.; Li, F.; Xue, B. The role of exfoliated kaolinite on crystallinity, ion conductivity, thermal and mechanical properties of poly(ethylene oxide)/kaolinite composites. *Polym. Bull.* **2017**, *74*, 3089–3108.
- (43) Liao, B.; Qiu, L.; Wang, D.; Bao, W.; Wei, Y.; Wang, Y. The behaviour of water on the surface of kaolinite with an oscillating electric field. *RSC Adv.* **2019**, *9*, 21793–21803.
- (44) Zhang, L.; Lu, X.; Liu, X.; Yang, K.; Zhou, H. Surface Wettability of Basal Surfaces of Clay Minerals: Insights from Molecular Dynamics Simulation. *Energy Fuels* **2016**, *30*, 149–160.
- (45) Xue, H.; Dong, Z.; Chen, X.; Tian, S.; Lu, S.; Lu, S. Simulation of Oil-Water Rock Wettability of Different Constituent Alkanes on Kaolinite Surfaces at the Nanometer Scale. *J. Nanosci. Nanotechnol.* **2021**, *21*, 225–233.
- (46) Dong, Z.; Xue, H.; Li, B.; Tian, S.; Lu, S.; Lu, S. Molecular Dynamics Simulations of Oil-Water Wetting Models of Organic Matter and Minerals in Shale at the Nanometer Scale. *J. Nanosci. Nanotechnol.* **2021**, *21*, 85–97.
- (47) Chen, G.; Li, C.; Lu, S.; Guo, T.; Wang, M.; Xue, Q.; Tian, Y.; Li, Z.; Sun, Y.; Liu, J.; Jiang, S. Critical factors controlling adsorption capacity of shale gas in Wufeng-Longmaxi formation, Sichuan Basin: Evidences from both experiments and molecular simulations. *J. Nat. Gas Sci. Eng.* **2021**, *88*, No. 103774.
- (48) Xiong, Y.; Cao, T.; Chen, Q.; Li, Z.; Yang, Y.; Xu, S.; Yuan, S.; Sjöblom, J.; Xu, Z. Adsorption of a Polyaromatic Compound on Silica Surfaces from Organic Solvents Studied by Molecular Dynamics

Simulation and AFM Imaging. *J. Phys. Chem. C* **2017**, *121*, 5020–5028.

(49) Xiong, Y.; Li, Z.; Cao, T.; Xu, S.; Yuan, S.; Sjöblom, J.; Xu, Z. Synergistic Adsorption of Polyaromatic Compounds on Silica Surfaces Studied by Molecular Dynamics Simulation. *J. Phys. Chem. C* **2018**, *122*, 4290–4299.

(50) Zhang, X.; Pang, X.; Jin, Z.; Hu, T.; Toyin, A.; Wang, K. Depositional model for mixed carbonate-clastic sediments in the Middle Cambrian Lower Zhangxia Formation, Xiaweidian, North China. *Adv. Geo-Energy Res.* **2020**, *4*, 29–42.

(51) Wang, S.; Feng, Q.; Javadpour, F.; Hu, Q.; Wu, K. Competitive adsorption of methane and ethane in montmorillonite nanopores of shale at supercritical conditions: A grand canonical Monte Carlo simulation study. *Chem. Eng. J.* **2019**, *355*, 76–90.

(52) Xiong, J.; Liu, X.; Liang, L.; Zeng, Q. Adsorption Behavior of Methane on Kaolinite. *Ind. Eng. Chem. Res.* **2017**, *56*, 6229–6238.

(53) Zhang, B.; Kang, J.; Kang, T. Effect of water on methane adsorption on the kaolinite (0 0 1) surface based on molecular simulations. *Appl. Surf. Sci.* **2018**, *439*, 792–800.

(54) Leebyn, C.; Egeniy, M. The effect of residual water content on preferential adsorption in carbon dioxide – methane – illite clay minerals: A molecular simulation study. *Fluid Phase Equilib.* **2020**, *504*, No. 112333.

(55) Frenkel, D.; Smit, B. *Understanding Molecular Simulation: From Algorithms to Applications*; Elsevier 2001, 1.

(56) Sharma, A.; Namsani, S.; Singh, J. K. Molecular simulation of shale gas adsorption and diffusion in inorganic nanopores. *Mol. Simul.* **2015**, *41*, 414–422.

(57) Seyyedattar, M.; Zendehboudi, S.; Butt, S. Molecular dynamics simulations in reservoir analysis of offshore petroleum reserves: A systematic review of theory and applications. *Earth-Sci. Rev.* **2019**, *192*, 194–213.

(58) Vatamanu, J.; Bedrov, D. Capacitive Energy Storage: Current and Future Challenges. *J. Phys. Chem. Lett.* **2015**, *6*, 3594–3609.

(59) Li, W.; Pang, X.; Snape, C.; Zhang, B.; Zheng, D.; Zhang, X. Molecular Simulation Study on Methane Adsorption Capacity and Mechanism in Clay Minerals: Effect of Clay Type, Pressure, and Water Saturation in Shales. *Energy Fuels* **2019**, *33*, 765–778.

(60) Croitoru, A.; Park, S.-J.; Kumar, A.; Lee, J.; Im, W.; MacKerell, A. D.; Aleksandrov, A. Additive CHARMM36 Force Field for Nonstandard Amino Acids. *J. Chem. Theory Comput.* **2021**, *17*, 3554–3570.

(61) Lennard-Jones, J. On the determination of molecular fields. II. From the equation of state of a gas. *Proc. R. Soc. A: Math. Phys. Eng. Sci.* **1924**, *106*, 463–477.

(62) York, D. M.; Darden, T. A.; Pedersen, L. G. The effect of long-range electrostatic interactions in simulations of macromolecular crystals: a comparison of the Ewald and truncated list methods. *J. Chem. Phys.* **1993**, *99*, 8345–8348.

(63) Shi, X.; Wu, W.; Zhou, S.; Tian, C.; Li, D.; Li, Y.; Cai, C.; Chen, Y. Adsorption characteristics and controlling factors of marine deep shale gas in southern Sichuan Basin China. *J. Nat. Gas Geosci.* **2022**, *7*, 61–72.

(64) Xie, W.; Wang, M.; Wang, H. Adsorption Characteristics of CH<sub>4</sub> and CO<sub>2</sub> in Shale at High Pressure and Temperature. *ACS Omega* **2021**, *6*, 18527–18536.

(65) Zhou, S.; Wang, H.; Li, B.; Li, S.; Sepehrnoori, K.; Cai, J. Predicting adsorbed gas capacity of deep shales under high temperature and pressure: Experiments and modeling. *Adv. Geo-Energy Res.* **2022**, *6*, 482–491.

(66) Zhang, G.; Nie, H.; Xuan, T. Evaluation of shale gas preservation conditions based on formation water index: A case study of Wufeng-Longmaxi Formation in Southeastern Chongqing. *Reserv. Eval. Dev.* **2021**, *11*, 47–55.